

Article

# Necessary Conditions for Running through a Flange by Using Planetary-Geared Magnetic Wheels

Masaru Tanida <sup>1</sup>, Kosuke Ono <sup>1</sup>, Takehiro Shiba <sup>2</sup> and Yogo Takada <sup>1,\*</sup>

<sup>1</sup> Department of Mechanical Engineering, Osaka Metropolitan University, Osaka 599-8531, Japan; so22059h@st.omu.ac.jp (M.T.); sg22620t@st.omu.ac.jp (K.O.)

<sup>2</sup> Measurement Industry Co., Ltd., Osaka 590-0056, Japan

\* Correspondence: takada@omu.ac.jp

**Abstract:** To discuss and consider the necessary conditions for magnetic-wheeled robots with planetary-geared magnetic wheels, this paper provides comparing static calculations about three orientations in running a flange with real experiments. SCPREM-I, a magnetic-wheeled robot, was developed for running through a flange from the bottom to the top. This robot has four magnetic wheels with a built-in planetary gearset. In experiments, however, the robot sometimes fails to run through a flange in three orientations. In this study, we statically analyze SCPREM-I to find the conditions necessary for running through the flange. We calculate the forces around the front and rear wheels in the three orientations. As a result, it has been found that the chassis of the SCPREM-I applies a forward force to the wheels when it runs through the flange. In addition, it has been found that the normal force of the A-Legs is balancing with the driving force of the wheels when the SCPREM-I fails to run through the flange.

**Keywords:** mobile robots; magnet wheels; force model



**Citation:** Tanida, M.; Ono, K.; Shiba, T.; Takada, Y. Necessary Conditions for Running through a Flange by Using Planetary-Geared Magnetic Wheels. *Robotics* **2024**, *13*, 72. <https://doi.org/10.3390/robotics13050072>

Academic Editor: Hicham Chaoui

Received: 23 March 2024

Revised: 2 May 2024

Accepted: 6 May 2024

Published: 8 May 2024



**Copyright:** © 2024 by the authors. Licensee MDPI, Basel, Switzerland. This article is an open access article distributed under the terms and conditions of the Creative Commons Attribution (CC BY) license (<https://creativecommons.org/licenses/by/4.0/>).

## 1. Introduction

Large-scale plant equipment and infrastructures should be inspected regularly for early detection of damage [1,2]. However, if large-scale inspection equipment or scaffolding is required, these inspections are costly, time-consuming, and dangerous for workers. Therefore, robots are required to inspect instead of humans [3–13].

Magnetic-wheeled robots are a type of adhesion that runs on steel structures with magnetic wheels [14–26]. Because this type of robot is equipped with permanent magnets for adhesion to structures, it does not consume electric power other than movement. Therefore, it can work for a longer time than drones that need to fly continuously. In addition, it can improve the payload capacity [13]. The robots also do jobs that require getting close to structures and inspecting them safely. Today, magnetic-wheeled robots are being actively studied in the area of control technology, such as three-dimensional positioning or sensing of running surface. Therefore, they are put to practical use in infrastructure and ship inspections. On the other hand, there is insufficient study on their ability and mechanisms to move on complex structures.

When the robots run on steel structures, they need to travel on a bolted splice part and complex three-dimensional paths. In particular, it is very difficult to move from the bottom to the top of the flanges.

The main reason why it is difficult to run on the flanges is the reaction torque of a motor and gravity. Even if the robots attempt to move from the bottom to the top of the flanges, the anti-torque and gravity push the robot down, as shown in Figure 1. Therefore, it is difficult to run through the flanges [27].

Planetary-geared magnetic wheels are devised for running on flanges [28]. The planetary gear mechanism that the wheel has built-in can reverse anti-torque, so this wheel assists in

running on the flanges. Furthermore, we built a four-wheeled robot, SCPREM-I, equipped with these wheels and conducted a running experiment on the flanges. As a result, SCPREM-I could break through a 15 mm thick flange with only forward movement. On the other hand, the robot sometimes could not move forward while driving. However, the specific conditions for success or failure in running through the flange are not known yet.

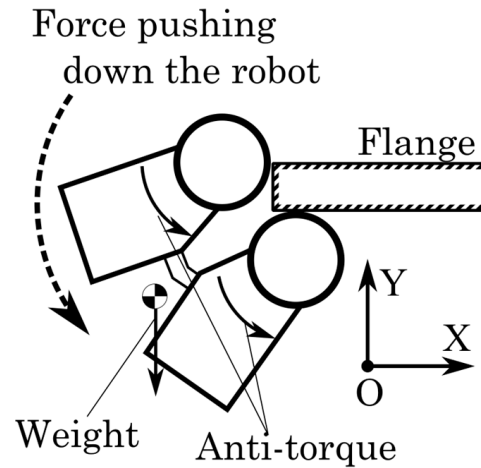


Figure 1. The magnetic-wheeled robot, which is stacked on the flange path.

In this study, static calculations of SCPREM-I running on the flange were performed to determine the conditions necessary for running through.

## 2. SCPREM-I

### 2.1. Planetary-Geared Magnetic Wheels

The external appearance of the planetary-gear magnetic wheel (PGMW) developed is shown in Figure 2, the internal structure is shown in Figure 3, and the main specifications are shown in Table 1. The wheel has a built-in planetary gear mechanism composed of a sun gear, planetary gears, an internal gear, and a planetary gear carrier.

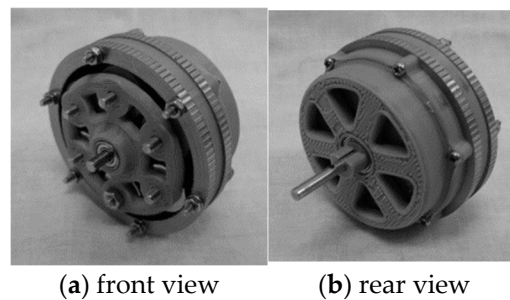


Figure 2. A planetary-gear magnetic wheel (PGMW).

Table 1. Specifications of the PGMW.

Parameter		Value
Diameter		52.0 mm
Mass		0.096 kg
Max magnetic force		34.7 N
Teeth number	Sun gear $Z_A$	18
	Planetary gear $Z_B$	12
	Internal gear $Z_C$	42
Reduction ratio $i = Z_C/Z_A$		7/3

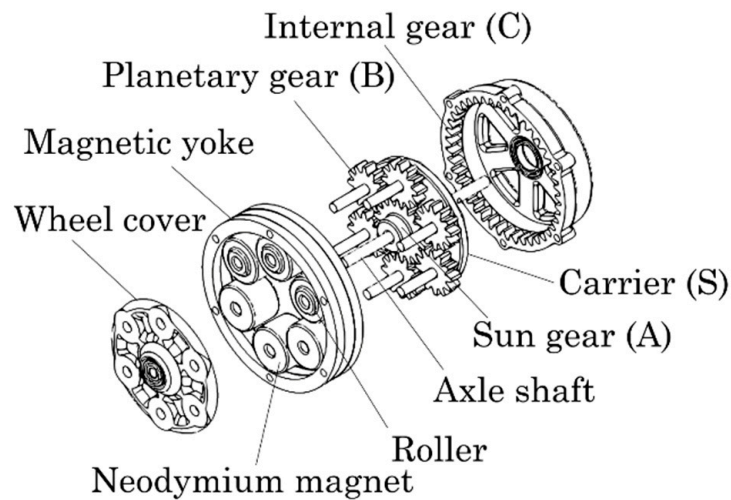


Figure 3. Inside of the PGMW.

When torque is applied to the axle (sun gear) in the CCW direction, the rim (internal gear) output torque is in the CW direction and the carrier output torque is in the CCW direction. When rotating either the carrier or the internal gear, the other needs to be fixed.

The PGMW is equipped with a bar-shaped part called the Assistant Leg (A-Leg). This part can rotate together with a planetary gear carrier in the wheel. As shown in Figure 4, when the sun gear drives in CCW, the carrier tries to rotate in CCW. However, if the tip of the A-Leg contacts the running surface, a normal force from the running surface prevents the A-Leg and the carrier from rotating. Therefore, the rim of the wheel can rotate in CW. In addition, the chassis applies anti-torque from the motor in the CW direction. Accordingly, the robot can run through the flange path without the anti-torque which pushes down the body.

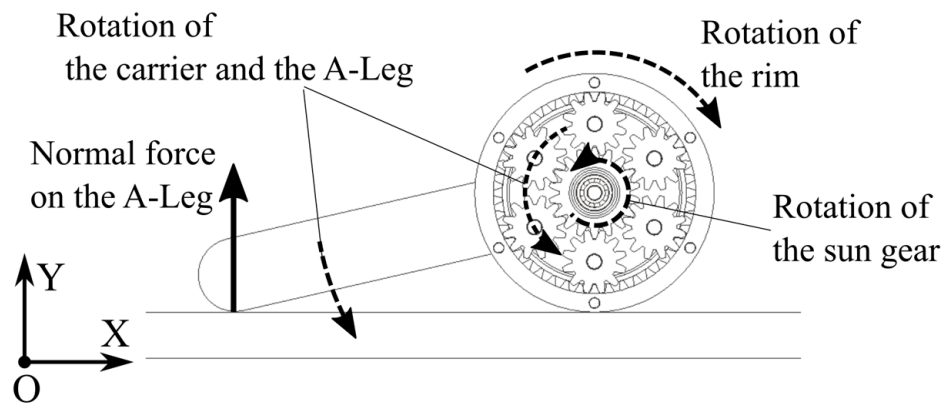
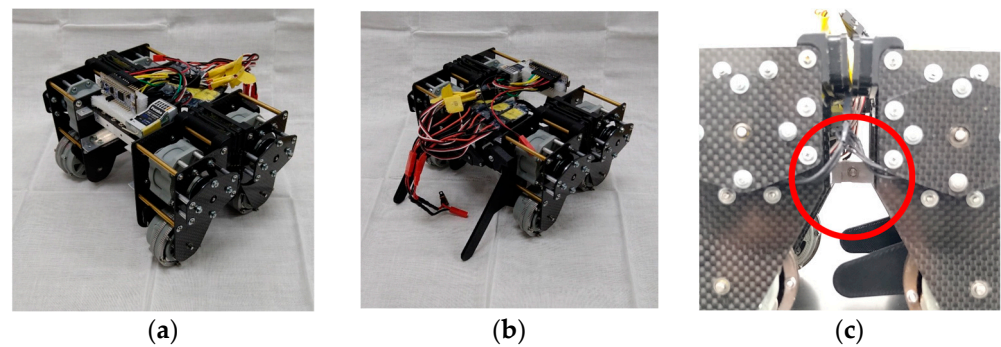


Figure 4. Movement of the PGMW and the A-Leg.

As another way to rotate the rim in the CW direction, the A-Leg can be fixed to the robot body. In this case, the body applies torque from not only the motor but also from the carrier.

### 2.2. Actual Equipment of SCPREM-I

SCPREM-I, as shown in Figure 5, is a magnetic-wheeled robot. This robot is equipped with four PGMWs, and all of the wheels have motors and gearboxes. All wheels can be driven forward by remote control from a radio transmitter. The chassis is divided into the front and rear parts, and they are connected by a hinge.



**Figure 5.** SCPREM-I. (a) Front view. (b) Rear view. (c) Hinge (a small block in the red circle).

As shown in Figure 6, the A-Legs with different shapes are unified with the front and rear wheels. The A-Legs on the rear (Figure 6a) can be fixed to the chassis by locking mechanisms. This mechanism can be switched between “Locked” and “Unlocked”. On the other hand, the A-Legs on the front (Figure 6b) can be “Locked” by partially touching on the chassis. When the tip of this A-Leg contacts the running surface and loses contact with the chassis, it can be “Unlocked”.

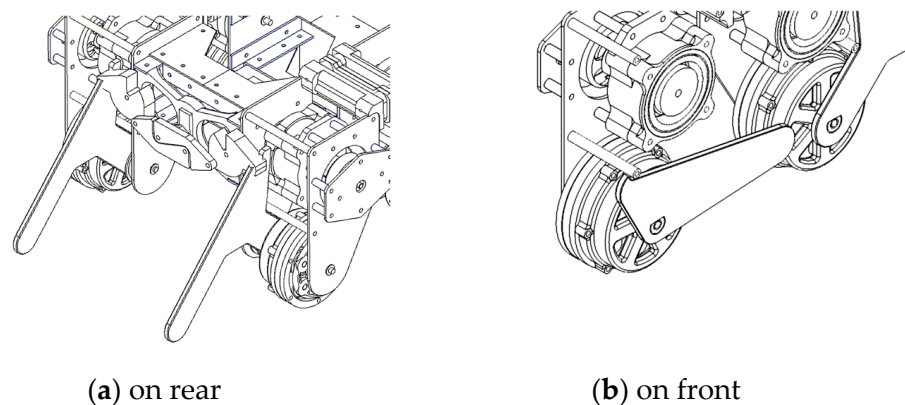


**Figure 6.** Assistant legs.

### 2.3. Running Experiment

A steel structure for running experiments is shown in Figure 7. The straight edge of this in the left front of the figure is the flange with a uniform thickness of 15 mm. SCPREM-I can run through this flange with only forward movement. A schematic diagram of running on the flange is shown in Figure 8. The driving procedure is shown below.

- (1) Move forward from the starting point (a) toward a side of the flange by four-wheel drive (b).
- (2) Bring the tip of the rear A-Legs into contact with the bottom surface of the flange and drive the rear wheel to push up the robot (c).
- (3) While pushing up the robot with the rear wheels, drive the front wheels to move forward (d).
- (4) The front wheel reaches the top of the flange. On the other hand, the rear wheel cannot move forward on the side (e).
- (5) When only the front wheel is moved forward, the tip of the front A-Legs contacts with the top surface of the flange (f).
- (6) When the front wheels are driven further, the front chassis pulls up the rear chassis (g).
- (7) The rear wheel is pulled up. The rear A-Legs are retracted by the rotation of the rim of the rear wheels (h).

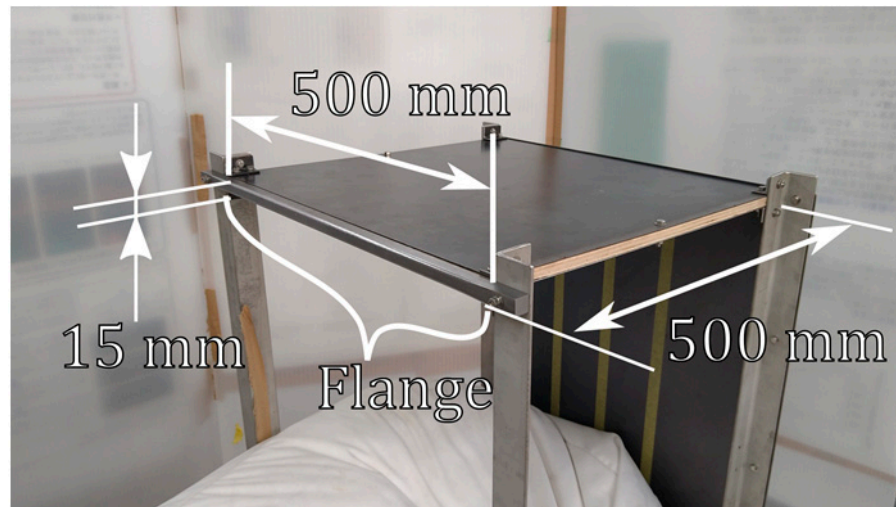


Figure 7. A steel structure for running experiments.

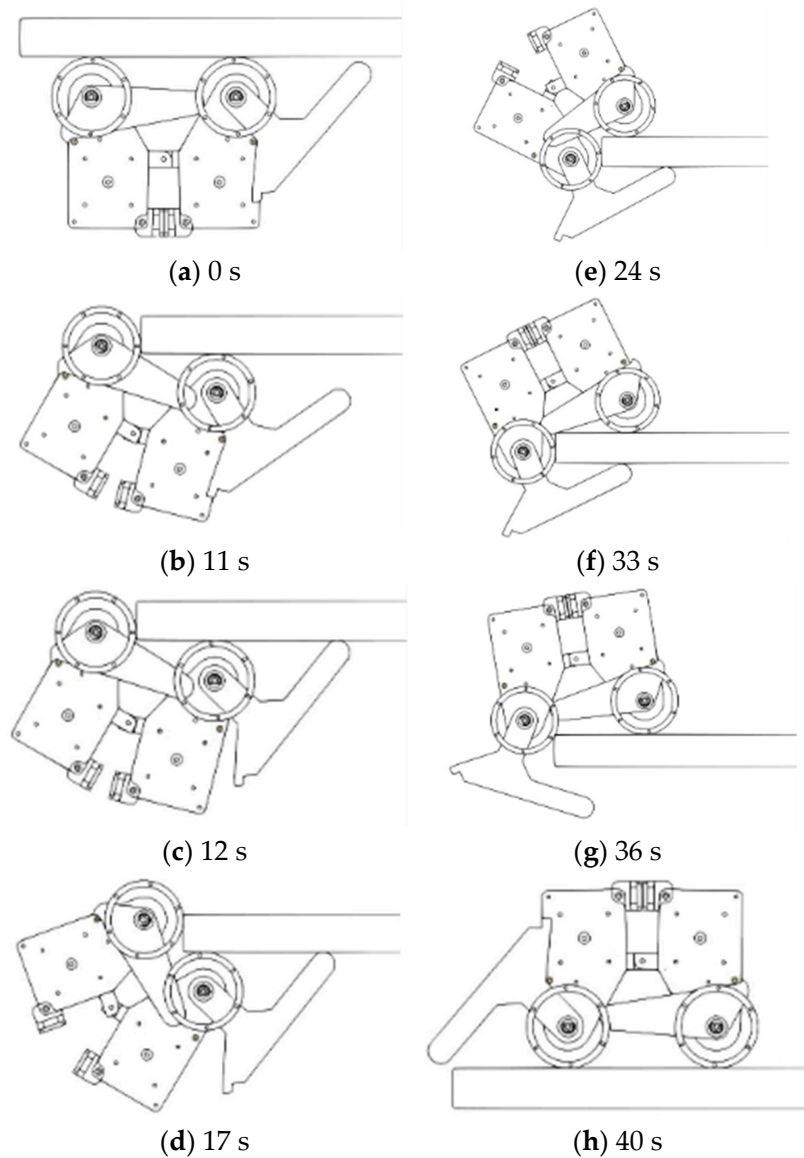


Figure 8. Schematic diagrams of SCPREM-I running on the flange path.

2.4. Problem

SCPREM-I can run through the flange by using the A-Legs. However, the robot sometimes cannot move forward in (d), (e), and (f). Figure 9 is a reproduction of the case where the SCPREM-I fails to run through the flange.

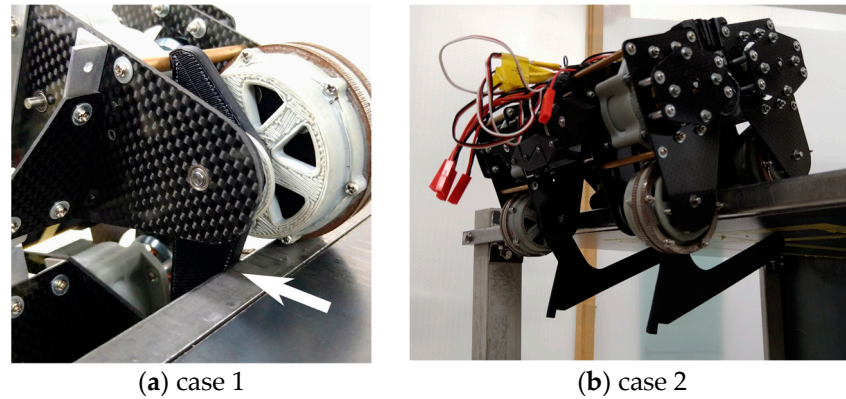


Figure 9. Reproduction of the case where the SCPREM-I fails to run through the flange. A white allow in (a) highlights a contacting point of the A-Leg and the corner of the running surface.

Figure 9a is the case where the front wheels cannot move in (d) and (e) in Figure 8. Figure 9b is the case where the robot cannot pull up the rear wheels in (f) from Figure 8. In both cases, the front wheels slip on the running surface and cannot move forward.

We can speculate that the reason for these cases is that the A-Legs are blocking the forward movement of the wheels with a strong normal force from the running surface. However, the specific relationship between these forces is not yet clear.

3. Static Characteristics of SCPREM-I

We analyzed equations of the front and rear wheels to find characteristics of SCPREM-I.

Hereinafter, the horizontal right direction is the positive X-axis direction, and the vertically upward direction is the positive Y-axis direction. Moreover, the counterclockwise direction is the positive direction of rotation and torque.

3.1. Geometric Definition

We describe a SCPREM-I model used in the calculations. In this model, the connected front and rear chassis are the same shape. A model of the chassis and wheels on one side is shown in Figure 10 using the subscript  $j$ . Here,  $j = 1$  indicates the front case, and  $j = 2$  indicates the rear case. The rotational axes of the wheels are the point  $O_j$ , and the axis of the hinge is the point  $O_3$ . The angle of the chassis is defined as the angle  $\theta_j$  to the X axis. Both the front and rear wheels have a radius of  $r_w$  and the length of the straight line  $O_jO_3$  is  $L_b$ .

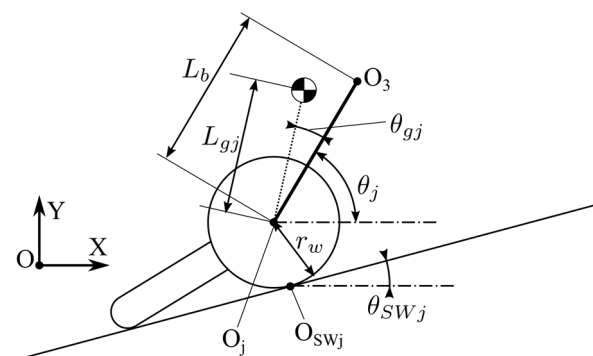
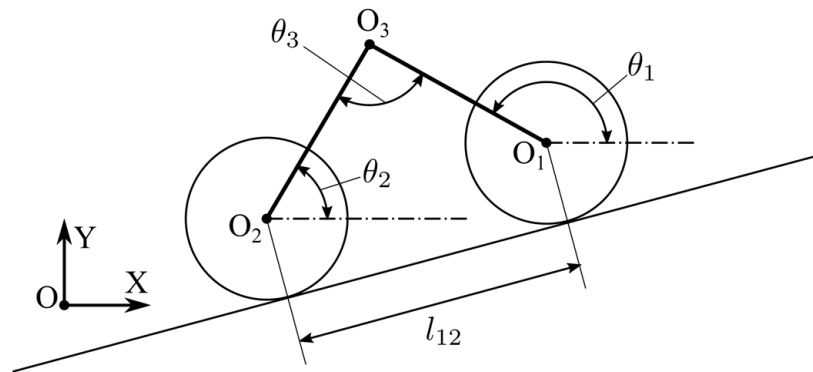


Figure 10. Geometric model of one side of the body of the robot.

The position of the gravity point of the chassis is expressed as the distance from point  $O_j$  and the angle to the straight line  $O_jO_3$ . Since the A-Legs are very light compared to the carrier shaft and neodymium magnets that rotate together, the gravity point of PGMW is assumed to be at point  $O_j$ .

A model of the robot with front and rear chassis is shown in Figure 11. In this figure, the chassis is shown as the line  $O_1O_3$  and  $O_2O_3$ . The angle formed by the two bodies is  $\theta_1 - \theta_2 = \theta_3$ . However, there is a stopper to prevent the distance between the front and rear wheels from becoming too wide, so  $\theta_3 \leq \theta_{3l} (< \pi)$ . Here,  $\theta_{3l}$  is the limit angle of the hinge.



**Figure 11.** Geometric model of front and rear chassis of the robot. The chassis is shown as the line  $O_1O_3$  and  $O_2O_3$ .

When defining the coordinates of the front and rear wheel axes as  $O_1(x_{O1}, y_{O1})$  and  $O_2(x_{O2}, y_{O2})$ , a wheelbase  $l_{12}$  is expressed with the following formula:

$$l_{12} = \sqrt{(x_{O1} - x_{O2})^2 + (y_{O1} - y_{O2})^2}. \tag{1}$$

$\theta_{SWj}$  is the angle that the surface touching the wheel makes with the X-axis.

We describe the A-Legs.  $P_{Lj}(x_{Lj}, y_{Lj})$  is the contact point of the A-Leg and the running surface. As shown in Figure 10, the A-Legs can touch in two ways. In Figure 12a, the tip of the A-Leg is touching on the running surface. In Figure 12b, however, a point on the A-Leg is touching on the corner of the running surface.

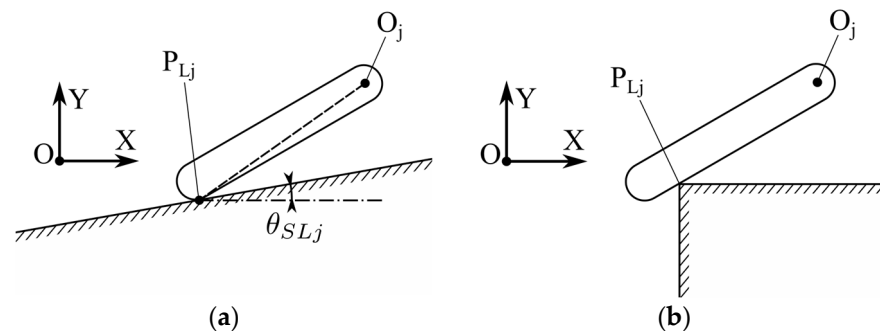


**Figure 12.** How the A-Legs contact the running surface. (a) The tip of the A-Leg touches on the running surface; (b) a point on the A-Leg touches on the corner of the running surface.

In the case of SCPREM-I, the A-Leg on the front wheels can use both methods of Figure 12a,b. However, the A-Leg on the rear wheels can use the method of Figure 12a because of the shape of the A-Leg.

As shown in Figure 12a,  $\theta_{SLj}$  is the angle that the surface touching with the A-Leg makes with the X-axis.

### 3.2. Mechanical Definition

We define the mechanical elements. Figure 13 shows the forces and moments applied on the front or rear wheels.  $m_{bj}$  is the mass of the chassis.  $m_{wj}$  is the mass of the rim.  $m_{Lj}$  is the combined mass of the A-Legs and carrier in the wheels.  $F_j$  is the frictional force received from the running surface.  $M_j, N_j$  are the adhesion force and normal force that the wheels receive from the running surface, respectively.  $f_{bj}$  is the translational force applied from the chassis to the wheels.  $f_{Lj}$  is the translational force applied from the A-Legs to the wheels. Inherently, the magnetic force is affected by the irregularity of the surface, moving speed, and so on. To simplify calculations, however, this study assumes that the robot runs on a smooth surface at low speed and the adhesion force  $N_j$  is constant. In addition, the rolling friction is weak because the rim of the wheels is made of SS400. Therefore, it is omitted for calculations.

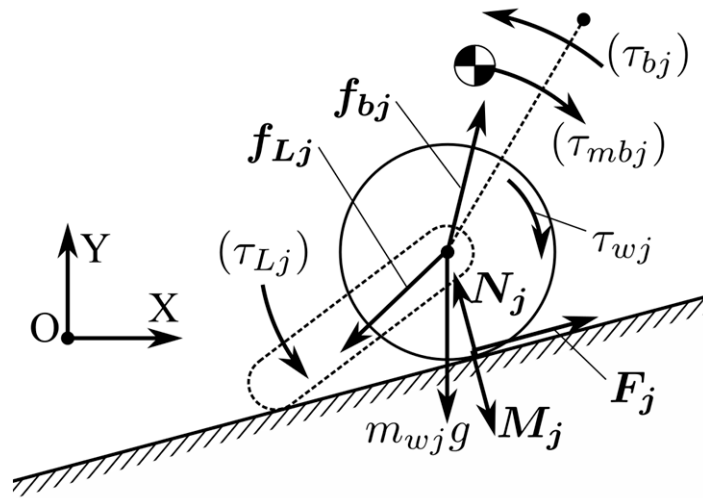


Figure 13. The roading situation of the wheel.

$\tau_{bj}, \tau_{Lj}$ , and  $\tau_{wj}$  are the torques applied to the chassis, the A-Legs, and the rim when motor torque  $\tau_j$  is applied to the drive shaft of the wheel.

For simplicity, the moment  $\tau_{mbj}$  around point  $O_j$  generated by the weight of the chassis is defined as follows:

$$\tau_{mbj} = -m_{bj}g \cdot L_{gj} \cdot \cos(\theta_{gj} + \theta_j). \tag{2}$$

### 3.3. Equation of the Chassis

We describe the balance of forces between the front and rear chassis. When the hinge rotates freely, the torque from one chassis is not applied to the other, but only the coupling force is applied. However, on  $\theta_3 = \theta_{3l} (< \pi)$ , the front and rear chassis unite, and the torque from one chassis is applied to the other.

We assume that the hinge can be switched between free rotation and fixed at any angle, and the forces applied from the chassis to the front and rear wheels are calculated for each.

Figure 14a shows the forces applied to the front and rear chassis when the hinge rotates freely. At this time,  $f_{bj}$  is obtained by using the following formula:

$$f_{b1} = \left[ \begin{array}{c} \frac{(\tau_{b1} + \tau_{mb1})\cos\theta_2 + (\tau_{b2} + \tau_{mb2})\cos\theta_1}{L_b \sin\theta_3} \\ \frac{(\tau_{b1} + \tau_{mb1})\sin\theta_2 + (\tau_{b2} + \tau_{mb2})\sin\theta_1}{L_b \sin\theta_3} - m_{b1}g \end{array} \right] \tag{3}$$

$$f_{b2} = \left[ \begin{array}{c} -\frac{(\tau_{b1} + \tau_{mb1})\cos\theta_2 + (\tau_{b2} + \tau_{mb2})\cos\theta_1}{L_b \sin\theta_3} \\ -\frac{(\tau_{b1} + \tau_{mb1})\sin\theta_2 + (\tau_{b2} + \tau_{mb2})\sin\theta_1}{L_b \sin\theta_3} - m_{b2}g \end{array} \right]. \tag{4}$$

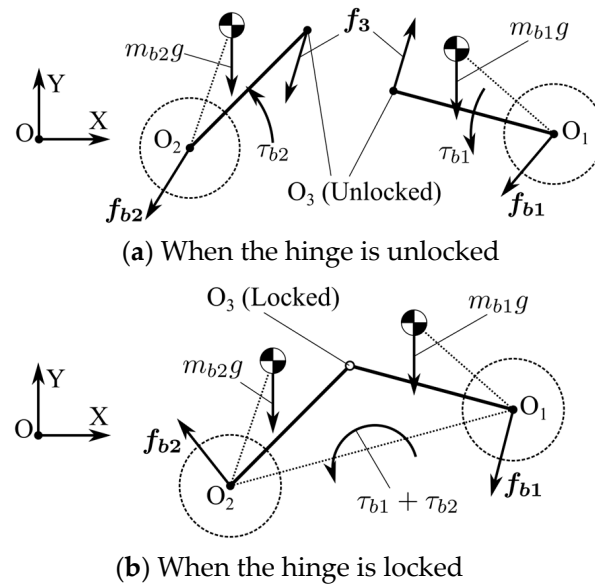


Figure 14. The forces and torques applied on the chassis.

Figure 14b shows the forces applied to the front and rear chassis when the hinge is in a fixed rotation. At this time,  $f_{bj}$  is obtained by using the following formula:

$$f_{b1} = \begin{bmatrix} -\frac{(\tau_{b1} + \tau_{b2})(y_{O1} - y_{O2})}{l_{12}^2} \\ \frac{(\tau_{b1} + \tau_{b2})(x_{O1} - x_{O2})}{l_{12}^2} + \frac{\tau_{mb1} + \tau_{mb2}}{x_{O1} - x_{O2}} - m_{b1}g \end{bmatrix} \quad (5)$$

$$f_{b2} = \begin{bmatrix} \frac{(\tau_{b1} + \tau_{b2})(y_{O1} - y_{O2})}{l_{12}^2} \\ -\frac{(\tau_{b1} + \tau_{b2})(x_{O1} - x_{O2})}{l_{12}^2} - \frac{\tau_{mb1} + \tau_{mb2}}{x_{O1} - x_{O2}} - m_{b2}g \end{bmatrix}. \quad (6)$$

### 3.4. Equation of the A-Legs

We describe a balance of force in the A-Legs. Figure 15 shows the A-Legs that touch on the running surface in  $\tau_{Lj} \geq 0$ .

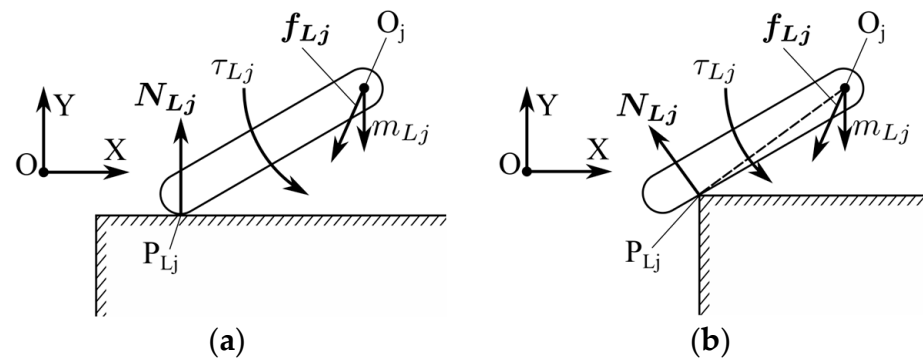


Figure 15. The forces and torques applied on the A-Legs. (a) The tip of the A-Leg touches on the running surface; (b) a point on the A-Leg touches on the corner of the running surface.

In the running experiments, the SCPREM-I with the A-Legs contacting on the running surface did not decrease the speed from when the A-Legs does not contact. It means that the friction force between the A-Legs and the running surface makes little difference to the movement of the robot. Therefore, we assume that there is no friction force between the A-Leg and the running surface.

When the tip of the A-Leg touches on the running surface, as shown in Figure 15a, the direction of  $N_{Lj}$  is perpendicular to the running surface.  $N_{Lj}$  is obtained as in the following formula:

$$N_{Lj} = \begin{bmatrix} -\frac{\tau_{Lj} \sin \theta_{SLj}}{(x_{Oj} - x_{Lj}) \cos \theta_{SLj} + (y_{Oj} - y_{Lj}) \sin \theta_{SLj}} \\ \frac{\tau_{Lj} \cos \theta_{SLj}}{(x_{Oj} - x_{Lj}) \cos \theta_{SLj} + (y_{Oj} - y_{Lj}) \sin \theta_{SLj}} \end{bmatrix}. \quad (7)$$

However, when the A-Legs touch on the corner, as shown in Figure 15b, the direction of  $N_{Lj}$  is perpendicular to the straight line  $O_j P_{Lj}$ .  $N_{Lj}$  is obtained as in the following formula:

$$N_{Lj} = \begin{bmatrix} -\frac{(y_{Oj} - y_{Lj}) \tau_{Lj}}{(x_{Oj} - x_{Lj})^2 + (y_{Oj} - y_{Lj})^2} \\ \frac{(x_{Oj} - x_{Lj}) \tau_{Lj}}{(x_{Oj} - x_{Lj})^2 + (y_{Oj} - y_{Lj})^2} \end{bmatrix}. \quad (8)$$

$f_{Lj}$  is the force that the A-Legs apply on the wheels. This force is obtained as in the following formula:

$$f_{Lj} = N_{Lj} + \begin{bmatrix} 0 \\ -m_{Lj} g \end{bmatrix}. \quad (9)$$

However, if the A-Leg does not touch on the running surface, then  $N_{Lj} = 0$ .

### 3.5. Equation of the Planetary Gearsets

In the planetary gear system, when one of a sun gear, an internal gear, and a carrier is rotated as input, the other two elements rotate as output [29]. Therefore, the balance of force in the PGMW should consider that the three elements (the sun gear, the rim, and the A-Leg) influence each other. When the motor torque  $\tau_j$  is applied on the sun gear, the interrelationships with the torque of the rim  $\tau_{wj}$  and the A-Leg  $\tau_{Lj}$  are obtained as in the following formula:

$$(1 + i)\tau_j + \left(1 + \frac{1}{i}\right)\tau_{wj} - \tau_{Lj} = 0. \quad (10)$$

When the A-Legs are fixed on the chassis, the rim rotates as an output part. The torques on each part are obtained, as shown below:

$$\tau_{Lj} = 0 \quad (11)$$

$$\tau_{bj} = i\tau_j \quad (12)$$

$$\tau_{wj} = -i\tau_j. \quad (13)$$

When the A-Leg does not touch the running surface, however, the rim and the A-Leg rotate as the output parts. Therefore, multiple equations are required to obtain the torque  $\tau_{Lj}$  and  $\tau_{wj}$ . The torque of the chassis is shown below:

$$\tau_{bj} = -\tau_j. \quad (14)$$

When the A-Leg does not touch the running surface, the normal force is  $N_{Lj} = 0$ , and the torque of the motor is used only for the rotation of the A-Legs. Therefore, the rim cannot have a driving force.

### 3.6. Equation of the Wheels

We describe the balance of the moment in the wheel. The equation of the force is shown below:

$$\tau_{wj} + F_j r_w = 0. \quad (15)$$

The equation of the force is shown below. Here,  $R(\theta)$  is a rotation matrix:

$$R(\theta_{SWj}) \begin{bmatrix} F_j \\ N_j - M_j \end{bmatrix} + \begin{bmatrix} 0 \\ -m_{wj}g \end{bmatrix} + f_{bj} + f_{Lj} = 0. \tag{16}$$

When the equations described above are solved, the friction force  $F_j$  can be obtained. This force is required for maintaining the orientation. Furthermore, this force represents the drag force that prevents the wheels from moving forward.

In addition, the actual driving force is obtained by the following formula, where  $\mu_w$  is the static friction coefficient of the wheels:

$$D_j = \begin{cases} -\tau_{wj}/r_w & (-\tau_{wj}/r_w \leq \mu_w N_{wj}) \\ \mu_w N_{wj} & (-\tau_{wj}/r_w > \mu_w N_{wj}) \end{cases}. \tag{17}$$

This calculation considers the moment when the wheels begin moving or slipping. Therefore, the  $\mu_w$  is used as the friction coefficient when the wheels have high driving force that causes slipping.

If the actual driving force  $D_j$  is higher than the drag force  $F_j$ , the wheel can move forward. In addition, in case of  $F_j < 0$ ,  $F_j$  is the force that pushes the wheels forward. We define the extra driving force  $F_{Ej}$  by the following formula:

$$F_{Ej} = D_j - F_j. \tag{18}$$

#### 4. Conditions for Successful Running

The running of the flange section of SCPREM-I is evaluated by using the static balance equation described in the previous chapter.

##### 4.1. Model of Flange Path

A model of the flange is shown in Figure 16. The corner on the lower left of the flange is the origin of a rectangular coordinate system. The horizontal right direction is the positive X-axis direction. The vertically upward direction is the positive Y-axis direction. The thickness of the flange is  $t$ . In addition, the real flange for experiments has its radius on the upper and lower corners. To simplify calculations, however, it is omitted and considered as corners with a right angle.

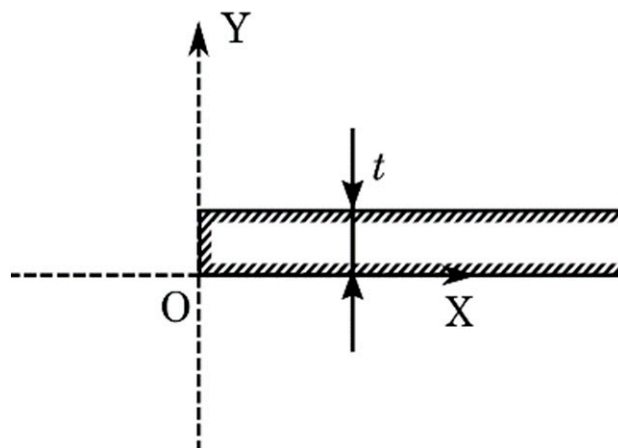


Figure 16. Two-dimensional model of the flange path.

##### 4.2. Orientations for Verification

Figure 17 shows three types of orientations when SCPREM-I runs on the flange. We mechanically verified these positions. The robot sometimes cannot move forward in these orientations. In this study, the parameters for each orientation are set as shown in Table 2.

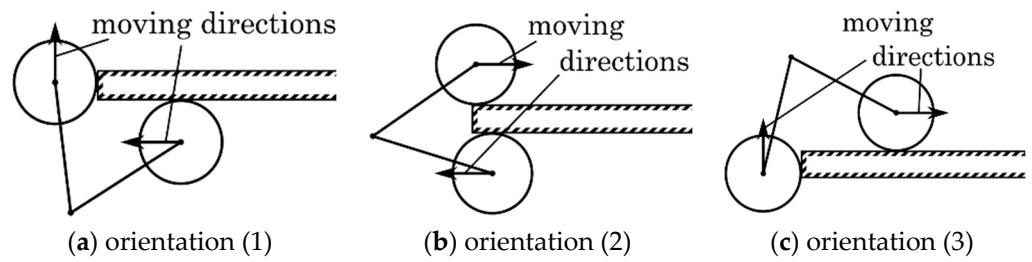


Figure 17. Typical orientations of SCPREM-I to be evaluated.

Table 2. Parameters for each orientation.

	(1)	(2)	(3)
$(\theta_{SW1}, \theta_{SW2})$	$(\frac{\pi}{2}, \pi)$	$(0, \pi)$	$(0, \frac{\pi}{2})$
$P_{L1}$	$(0, 0)$	$(0, t)$	$(x_{L1}, t)$
$P_{L2}$	$(x_{L2}, 0)$	$(x_{L2}, 0)$	$(x_{L2}, 0)$
Front leg	Locked	Locked	Unlocked
Rear leg	Unlocked	Unlocked	Unlocked
Hinge	Unlocked	Unlocked	Locked

Orientation (1)

In Figure 17a, the front wheels move up on the side. Also, the rear wheels move forward on the bottom. In this position, if the front A-Leg touches the lower corner, the robot cannot move forward due to the slipping wheels. The force and torque applied on the wheels in this orientation is shown in Figure 18.

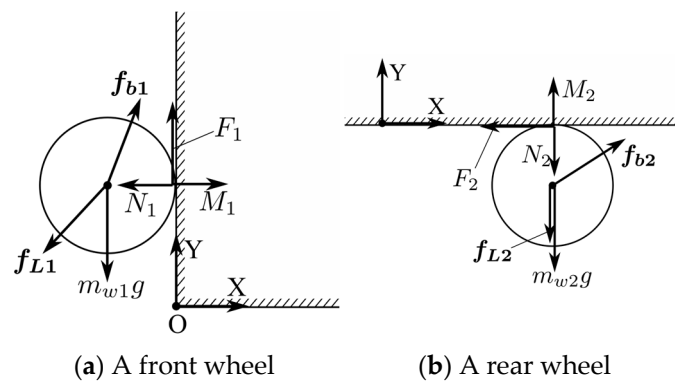


Figure 18. The force and torque applied on the wheels when in orientation (1).

Orientation (2)

In Figure 17b, the front wheels move forward on the top. Also, the rear wheels move forward on the bottom. In this position, when the front A-Leg touches the upper corner, the robot cannot move forward due to slipping wheels. In addition, this orientation is not shown in Figure 8, but the SCPREM-I has this orientation as it transitions from (d) to (e). The force and torque applied on the wheels in this orientation is shown in Figure 19.

Orientation (3)

In Figure 17c, the front wheels move forward on the top. Also, the rear wheels move up on the side. In this position, when the front A-Legs do not touch the running surface, the robot cannot move forward due to slipping wheels. Also, the rear A-Legs do not touch the running surface because the robot moves forward using only front-wheel drive. The force and torque applied on the wheels in this orientation is shown in Figure 20.

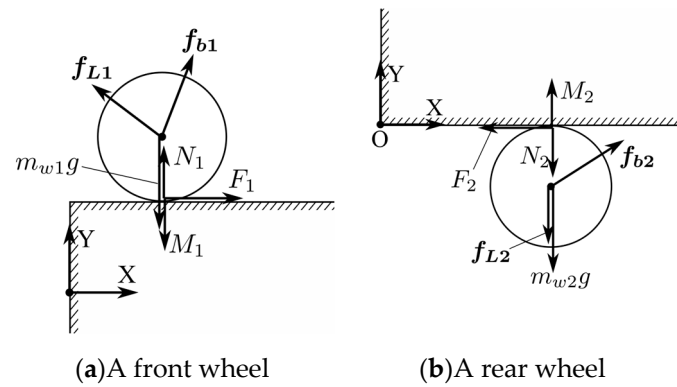


Figure 19. The force and torque applied on the wheels when in orientation (2).

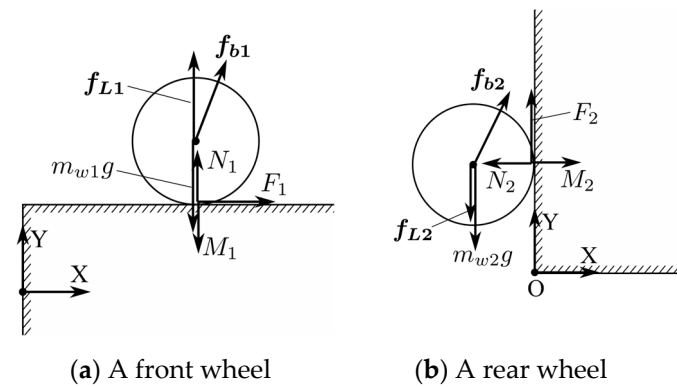


Figure 20. The force and torque applied on the wheels when in orientation (3).

4.3. Viewpoints of the Calculation Results

The calculation results are shown in a bubble chart with  $\tau_1$  on the horizontal axis and  $\tau_2$  on the vertical axis, as shown in Figure 21. The area of the circle is proportionate to  $F_{Ej}$ . The area of the circle on the lower left indicates 50 N of force magnitude. However, if  $|F_{Ej}|$  is less than 0.1 N, the area is shown as dots, which indicates 0.1 N. Also, a circle with a colored interior indicates a positive value, and a circle with a white interior indicates a negative value. The colors of the circles indicate the following:

Orange:  $F_j > 0$ ;

Yellow:  $F_j < 0$ ; this means that the chassis has the effect of pushing the front wheels or pulling the rear wheels.

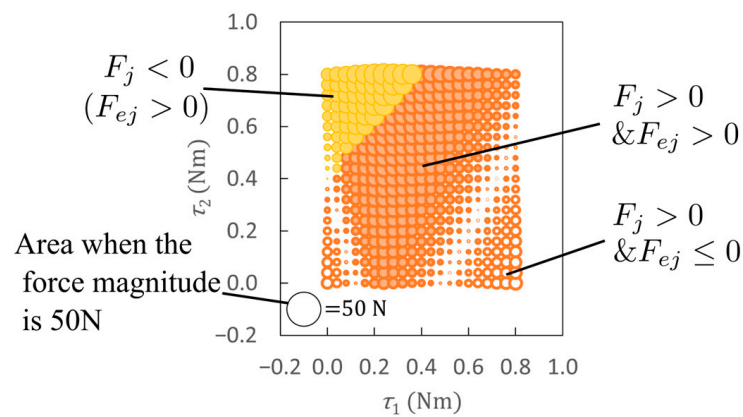


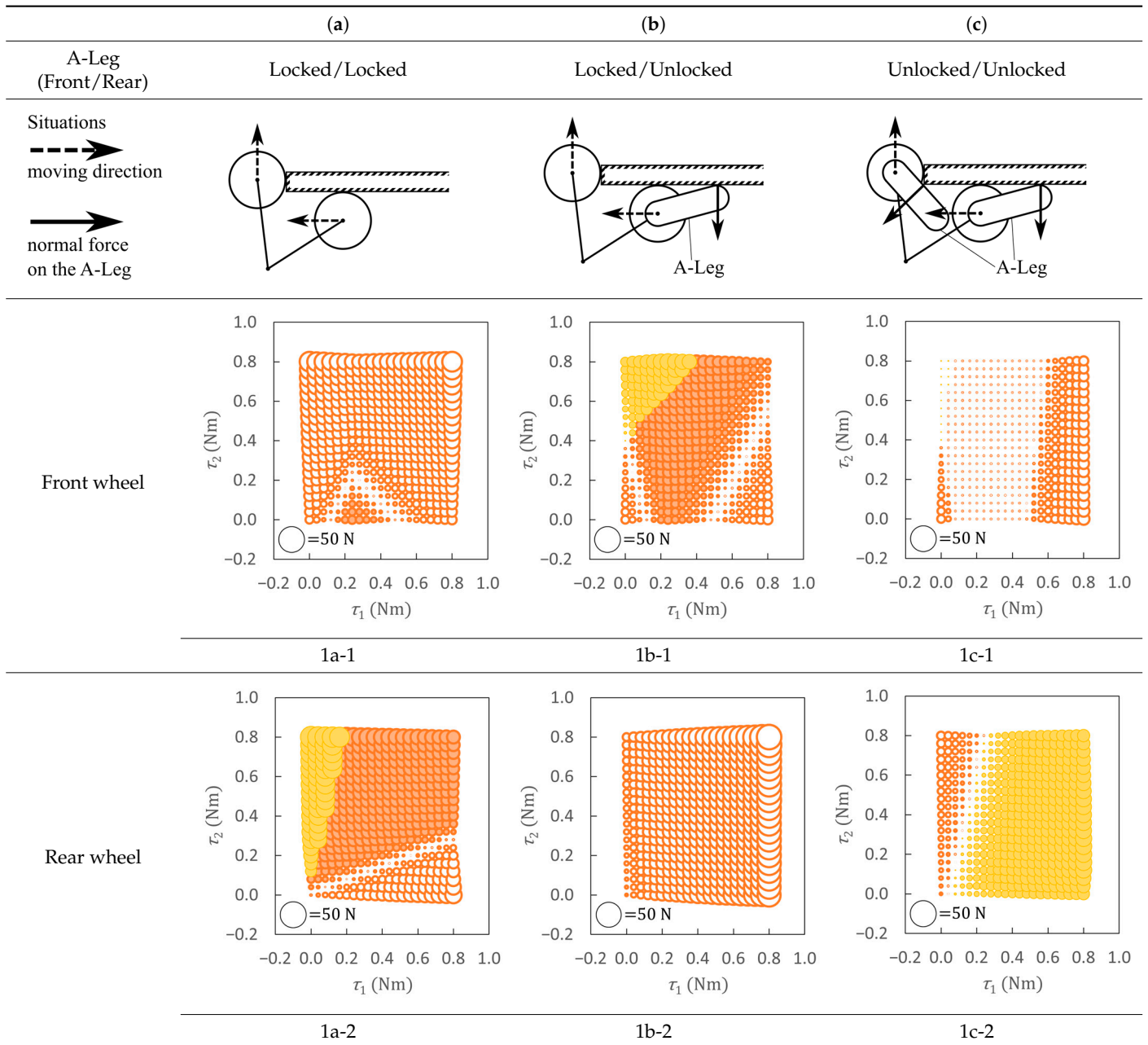
Figure 21. An example of calculation results.

4.4. Results for Each Orientation

4.4.1. Orientation (1)

Table 3 shows the calculation results for orientation (1).

Table 3. Calculation results for orientation (1).



The left column (a) from Table 3 shows the calculation results when the front and rear A-Legs are fixed. The front wheels cannot move forward when  $\tau_2$  exceeds approximately 0.3 Nm. On the other hand, the rear wheels can move forward when it has rear-wheel drive. However, if only the rear wheels move forward, the robot is not able to move forward to touch the front wheels.

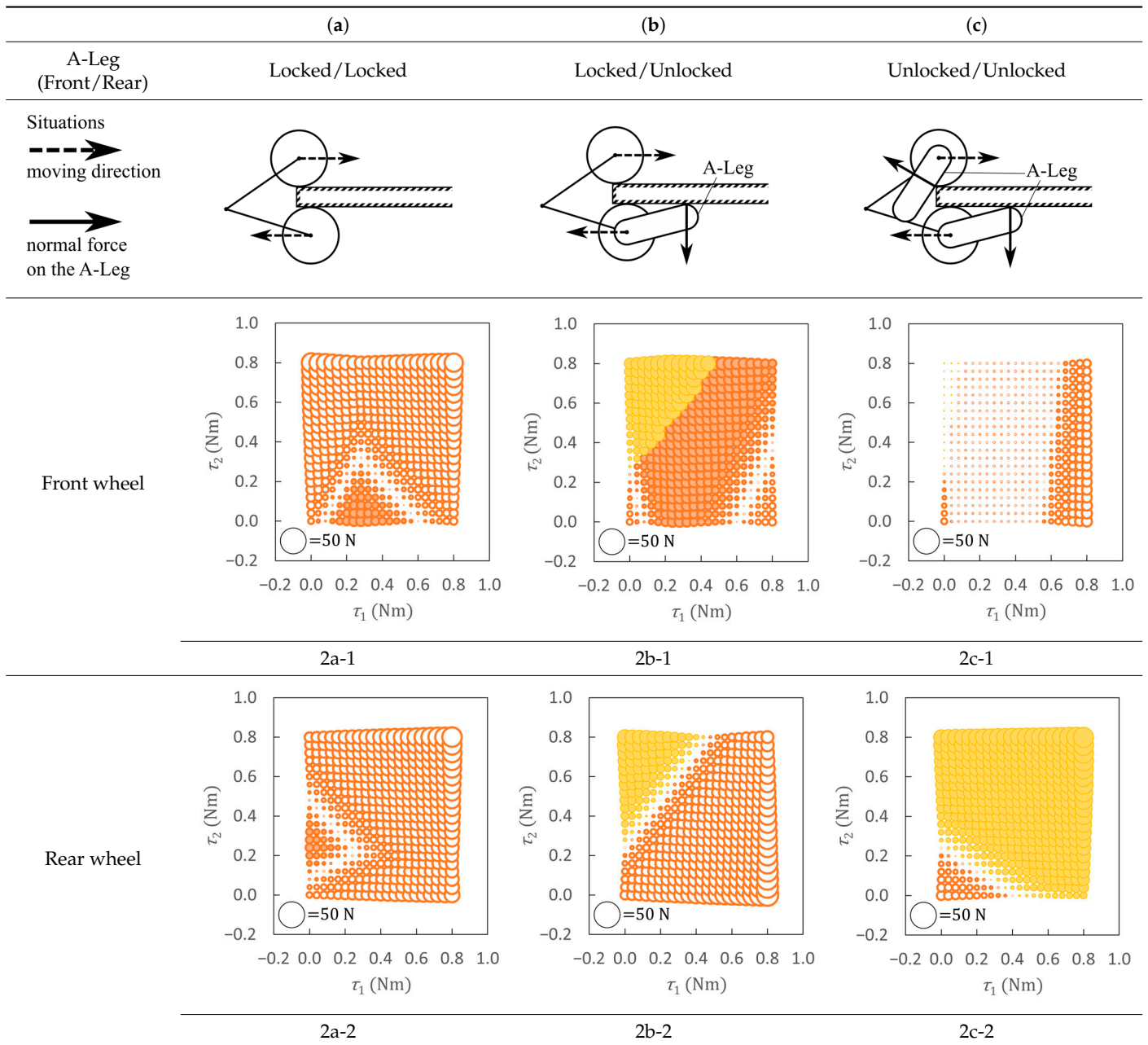
The middle column (b) from Table 3 shows the result when only the rear A-Legs are used. The front wheels can move forward over a wide range. Also, when  $\tau_2$  is sufficiently higher than  $\tau_1$ , the front chassis can push up the front wheel.

The right column (c) from Table 3 shows the results when the front and rear A-Legs are used. The front wheels cannot move forward in all areas. When  $\tau_1$  is sufficiently higher than  $\tau_2$ , the rear wheels can move forward by the rear chassis pulling.

4.4.2. Orientation (2)

Table 4 shows the calculation results for orientation (2).

**Table 4.** Calculation results for orientation (2).



The left column (a) from Table 4 shows the results when the front and rear A-Legs are fixed. Both front and rear wheels can move forward only in a small area.

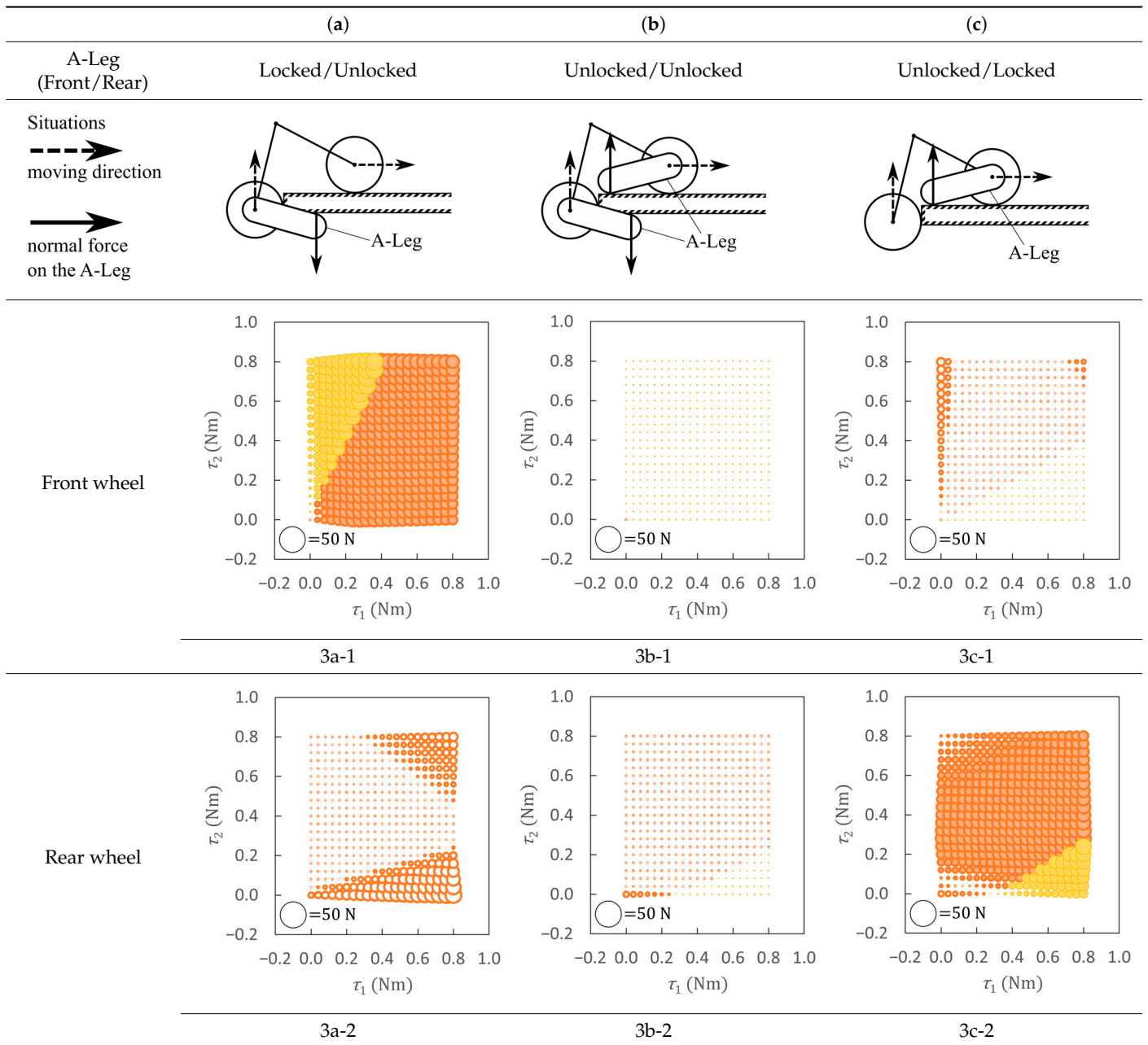
The middle column (b) from Table 4 shows the result when only the rear A-Legs are used. Unlike (a), the front wheels can move forward over a wide range. If  $\tau_2$  is increased, the rear wheels are also pulled with the chassis and move forward.

The right column (c) from Table 4 shows the results when the front and rear A-Legs are used. The front wheels cannot move forward in all areas. On the other hand, with rear-wheel drive, the rear wheels can move forward due to the pulling force of the chassis. Therefore, in orientation (2), the front and rear wheels originally prevent each other from moving forward, but it is possible to run with the rear A-Legs.

4.4.3. Results for Orientation (3)

Table 5 shows the calculation results for orientation (3).

Table 5. Calculation results for orientation (3).



The left column (a) from Table 5 shows the results when only the rear A-Legs are used. The  $F_{Ej}$  values of the rear wheels (3a-2) are spread over a wide range. Therefore, it is difficult to move forward in all areas. On the other hand, the front wheels (3a-1) can move forward

over a wide range. However, if only the front wheels move forward, the front wheels slip, or the hinge will be broken. Therefore, it is impossible to break through this position.

The middle column (b) from Table 5 shows the results when the front and rear A-Legs are used. When the robot is front-wheel drive, the rear wheels (3b-2) try to be pulled up by the rear chassis, but the force is weak. Also, both the forces of the front and rear wheels are balanced over a wide range. Therefore, it is difficult to move forward.

The right column (c) from Table 5 shows the results when only the front A-Legs are used. There is an area in which the rear wheels (3c-2) can move forward with rear-wheel drive. In addition, when the front wheels are driven, the chassis pulls up the rear wheels.

Therefore, if the rear A-Legs are used in orientation (3), the rear wheel cannot move forward. However, it is possible to break through this orientation by fixing the rear A-Legs and using the front A-Legs.

### 5. Comparison with Real SCPREM-I

#### 5.1. Comparison with the Running Experiments

The results in the previous chapter are compared with the real running experiments. Table 6 compares the states of the robot in each orientation with the state determined to be able to run in the calculation. In addition, this table includes the rate of success/failure for running in each orientation. This rate was calculated by running the previous experiments 38 times. For example, SCPREM-I stopped in orientation (1) in three out of thirty-eight cases. Therefore, the rates of success and failure in orientation (2) are calculated from the results of 35 cases of running through the orientation (1).

**Table 6.** The states of the robot in each orientation.

		(1)	(2)	(3)
Ideal situation in calculation		(b)	(b)	(c)
Situation in SCPREM-I	Success	(b) 35/38 (92%)	(b) 32/35 (91%)	(b) 24/32 (75%)
	Failure	(c) 3/38 (7.9%)	(c) 3/35 (8.6%)	(a) 8/32 (25%)

In the calculations, it has been found that situation (b) is the best for running in orientation (1). SCPREM-I using rear A-Leg (situation (b)) could run through orientation (1) 92% of the time. Similarly, situation (b) in orientation (2) is ideal in the calculation, and SCPREM-I succeeded in running through with a high rate of 91%. In orientations (1) and (2), the front wheels stopped moving forward when the front A-Leg touched the flange. This is consistent with the calculation result in situation (c). Furthermore, the calculation results show that the cause is that the driving force balances with the drag force.

In the driving experiment, in orientation (3), the front A-Legs were used to pull up the rear wheels with front-wheel drive. However, the front wheels often slipped and failed to pull up the rear wheels. This condition corresponds to situation (b). In the experiments, the rate of failure running in orientation (3) is 25% higher than orientations (1) and (2).

According to (3b-2) from Table 5, the rear chassis tries to pull up the rear wheels, but the driving force balances with the drag force. Therefore, it is impossible to move forward from a stationary state. However, if the wheels have an initial speed, uniform motion is possible. Therefore, it seems that SCPREM-I can pull up the rear wheels successfully when they have initial speed. Nevertheless, according to the calculation results, situation (c) seems to be better than situation (b) for running through in orientation (3).

#### 5.2. Experiments Based on the Calculation

According to the calculation results, if the rear wheel A-Legs are fixed in orientation (3), the rear wheel can move forward. We verified whether this is correct through the running experiments.

We fixed the rear A-Legs and the carrier to the chassis. Then, we put it on the experimental running route in orientation (3) and moved forward. The running processes are shown in Figure 22. It is shown that the rear wheels are pulled up and the front wheels hardly move in place. In all 10 running experiments, the rear wheels were able to move forward to the top of the flange. Therefore, this method can run with a higher success rate than the conventional SCPREM-I method.

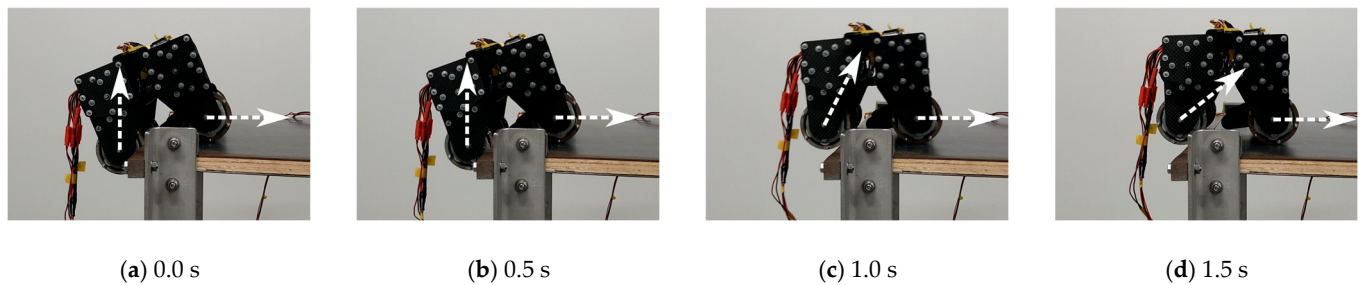


**Figure 22.** Running process in orientation (3) with situation (c). The moving directions of the wheels are shown in the figures as the white arrow.

## 6. Conclusions

In this study, we considered whether the SCPREM-I can move forward in three different orientations during the flange section by statistically calculating the extra driving force of the wheels.

The results showed that the PGMW with the A-Legs make it possible to move the wheels forward in orientations (1) and (2). The results are consistent with the performed experiments, which showed that the success rate is about 90%. Furthermore, based on the calculation results, when the rear A-Legs were fixed in orientation (3), the possibility of lifting the rear wheels improved. The experiments also showed a success rate of 100% across 10 test cases. In short, we analyzed the characteristics of PGMW in running through the flange, and obtained knowledge about the running procedure of SCPREM-I.

By not only the experiments with the SCPREM-I but also the calculations, it was suggested that the PGMWs give magnetic-wheeled robots the ability to run through the flange. The future robot could also be given the ability to lock the A-Leg in orientation (3), which would increase the success rate of running through the flange. Furthermore, if the robot has the ability (sensors and program) to control the torques of all wheels while keeping track of its orientations, it will realize driving methods that always make effective use of the A-Leg.

Even in recent studies for running on complex structures, almost no robot had attempted to solve the physical difficulties of running on the flange [18–26]. The outcomes of this study will allow these robots to choose their behaviors more flexibly. Furthermore, the technology for three-dimensional movement with magnets is needed not only for inspection but also for complex transfer operations in storage environments [30]. In short, this study allows magnetic-wheeled robots to expand their field of activity into new or difficult areas.

**Author Contributions:** Conceptualization, M.T.; data curation, M.T.; formal analysis, Y.T.; funding acquisition, T.S.; methodology, M.T.; project administration, Y.T.; supervision, Y.T.; validation, M.T. and K.O.; investigation, M.T.; writing—original draft preparation, M.T.; writing—review and editing, M.T., K.O., T.S. and Y.T. All authors have read and agreed to the published version of the manuscript.

**Funding:** This research received no external funding.

**Data Availability Statement:** Data are contained within the article.

**Conflicts of Interest:** Author Takehiro Shiba was employed by the company Measurement industry Co., Ltd. The remaining authors declare that the research was conducted in the absence of any commercial or financial relationships that could be construed as a potential conflict of interest.

## References

1. Hao, S. I-35W Bridge Collapse. *J. Bridge Eng.* **2010**, *15*, 608–614. [[CrossRef](#)]
2. Salem, H.M.; Helmy, H.M. Numerical investigation of collapse of the Minnesota I-35 bridge. *Eng. Struct.* **2014**, *59*, 635–645. [[CrossRef](#)]
3. Lee, W.; Hirose, S. Contacting Surface-Transfer Control for Reconfigurable Wall-Climbing Robot Gunryu III. *J. Robot. Mechatron.* **2013**, *25*, 439–448. [[CrossRef](#)]
4. Almadhoum, R.; Taha, T.; Seneviratne, L.; Dias, J.; Cai, G. A Survey on Inspecting Structures Using Robotic Systems. *Int. J. Adv. Robot. Syst.* **2016**, *13*, 76–81. [[CrossRef](#)]
5. Ham, Y.; Han, K.K.; Lin, J.J.; Golparvar-Fard, M. Visual monitoring of civil infrastructure systems via camera-equipped Unmanned Aerial Vehicles (UAVs): A review of related works. *Vis. Eng.* **2016**, *4*, 1. [[CrossRef](#)]
6. Gillins, M.N.; Gillins, D.T.; Parrish, C. Cost-Effective Bridge Safety Inspections Using Unmanned Aircraft Systems (UAS). In Proceedings of the Geotechnical and Structural Engineering Congress, Phoenix, AZ, USA, 14 February 2016. [[CrossRef](#)]
7. Ge, D.; Tang, Y.; Ma, S.; Matsuno, T.; Ren, C. A Pressing Attachment Approach for a Wall-Climbing Robot Utilizing Passive Suction Cups. *Robotics* **2020**, *9*, 26. [[CrossRef](#)]
8. Samarathunga, A.I.; Piyasundara, N.; Wanigasooriya, A.I.; Kumara, B.S.; Vithanage, V.P.; Chathuranga, D.S. A Robotic Platform for Aircraft Composite Structure Inspection Using Thermography. *Robotics* **2022**, *11*, 62. [[CrossRef](#)]
9. Nguyen, S.T.; La, H.M. A Climbing Robot for Steel Bridge Inspection. *J. Intell. Robot. Syst.* **2021**, *102*, 75. [[CrossRef](#)]
10. Li, J.; Li, B.; Dong, L.; Wang, X.; Tian, M. Weld Seam Identification and Tracking of Inspection Robot Based on Deep Learning Network. *Drones* **2022**, *6*, 216. [[CrossRef](#)]
11. Ekkachai, K.; Leelasawassuk, T.; Chaopramualkul, W.; Komin, U.; Kwansub, P.; Bunnun, P.; Komeswarakul, P.; Tantaworrasslip, A.; Seekhao, P.; Nithi-uthai, S.; et al. Development of the generator inspection vehicle and the inspection equipment. *J. Field Robot.* **2022**, *39*, 1033–1053. [[CrossRef](#)]
12. Jiang, Z.; Chen, B.; Ju, Z.; Li, Y.; Xu, Y.; Zhao, Y. Design and analysis of a wall-climbing robot for water wall inspection of thermal power plants. *J. Field Robot.* **2023**, *40*, 1003–1013. [[CrossRef](#)]
13. Shunsuke, N.; Mohan, R.E. A Survey of Wall Climbing Robots: Recent Advances and Challenges. *Robotics* **2016**, *5*, 14. [[CrossRef](#)]
14. Tâche, F.; Pomerleau, F.; Caprari, G.; Siegwart, R. Three-Dimensional Localization for the MagneBike Inspection Robot. *J. Field Robot.* **2010**, *28*, 180–203. [[CrossRef](#)]
15. Eich, M.; Vögele, T. Design and control of a lightweight magnetic climbing robot for vessel inspection. In Proceedings of the 2011 19th Mediterranean Conference on Control & Automation (MED), Corfu, Greece, 20–23 June 2011; pp. 1200–1205.
16. Wang, R.; Kawamura, Y. An Automated Sensing System for Steel Bridge Inspection Using GMR Sensor Array and Magnetic Wheels of Climbing Robot. *J. Sens.* **2016**, *2016*, 8121678. [[CrossRef](#)]
17. La, H.M.; Dinh, T.H.; Pham, N.H.; Ha, Q.P.; Pham, A.Q. Automated Robotic Monitoring and Inspection of Steel Structures and Bridges. *Robotica* **2018**, *37*, 947–967. [[CrossRef](#)]
18. Pham, A.Q.; La, H.M.; La, K.T.; Nguyen, M.T. A Magnetic Wheeled Robot for Steel Bridge Inspection. In *Advances in Engineering Research and Application*; Sattler, K.U., Nguyen, D., Vu, N., Tien Long, B., Puta, H., Eds.; ICERA 2019, Lecture Notes in Networks and Systems; Springer: Cham, Switzerland, 2019; Volume 104, pp. 11–17. [[CrossRef](#)]
19. Noh, M.; Kwon, E.; Park, S.H.; Park, Y.-W. Modeling of Attractive Force by Magnetic Wheel Used for Mobile Robot. *Actuators* **2020**, *9*, 67. [[CrossRef](#)]
20. Nguyen, S.T.; Nguyen, H.; Bui, S.T.; Ho, V.A.; Ngo, T.D.; La, H.M. An Agile Bicycle-like Robot for Complex Steel Structure Inspection. In Proceedings of the 2022 International Conference on Robotics and Automation (ICRA), Philadelphia, PA, USA, 23–27 May 2022; pp. 157–163. [[CrossRef](#)]
21. Pshenin, V.; Liagova, A.; Razin, A.; Skorobogatov, A.; Komarovskiy, M. Robot Crawler for Surveying Pipelines and Metal Structures of Complex Spatial Configuration. *Infrastructures* **2022**, *7*, 75. [[CrossRef](#)]
22. Thung-Od, K.; Kanjanawanishkul, K.; Maneewarn, T.; Serhaput, T.; Boonyaprapasorn, A. An In-Pipe Inspection Robot with Permanent Magnets and Omnidirectional Wheels: Design and Implementation. *Appl. Sci.* **2022**, *12*, 1226. [[CrossRef](#)]
23. Pham, A.Q.; Motley, C.; Nguyen, S.T.; La, H.M. A Robust and Reliable Climbing Robot for Steel Structure Inspection. In Proceedings of the 2022 IEEE/SICE International Symposium on System Integration (SII), Narvik, Norway, 9–12 January 2022; pp. 336–343. [[CrossRef](#)]
24. Zhang, X.; Zhang, M.; Jiao, S.; Zhang, X.; Li, M. Optimization Design and Parameter Analysis of a Wheel with Array Magnets. *Symmetry* **2023**, *15*, 962. [[CrossRef](#)]
25. Xuan, Z.; Zhang, M.; Jiao, S.; Sun, L.; Li, M. Design and Optimization of the Wall Climbing Robot for Magnetic Particle Detection of Ship Welds. *J. Mar. Sci. Eng.* **2024**, *12*, 610. [[CrossRef](#)]
26. Nguyen, S.T.; La, K.T.; La, H.M. Agile robotic inspection of steel structures: A bicycle-like approach with multisensor integration. *J. Field Robot.* **2024**, *41*, 396–419. [[CrossRef](#)]

27. Kobayashi, S.; Nakajima, K.; Song, H.; Takada, Y.; Shiba, T. Consideration of Method for Traveling through a Flange Path in Terms of Magnetic-Wheeled Bridge Inspection Robot with High Loading Capacity. In Proceedings of the JSME annual Conference on Robotics and Mechatronics Conference Digest, Osaka, Japan, 6–8 June 2021. [[CrossRef](#)]
28. Tanida, M.; Ono, K.; Kobayashi, S.; Shiba, T.; Takada, Y. Study of Magnetic Wheels with Planetary Gears Which Make Running on Flange Paths Easy for Magnetic Wheeled Robot. *J. Robot. Soc. Jpn.* **2024**, *42*, 64–73. [[CrossRef](#)]
29. Koganezawa, K. Active/Passive Hybrid Mechanism by Using Planetary Gear System. *J. Robot. Soc. Jpn.* **2011**, *29*, 502–505. [[CrossRef](#)]
30. Seriani, S.; Scalera, L.; Caruso, M.; Gasparetto, A.; Gallina, P. Upside-Down Robots: Modeling and Experimental Validation of Magnetic-Adhesion Mobile Systems. *Robotics* **2019**, *8*, 41. [[CrossRef](#)]

**Disclaimer/Publisher’s Note:** The statements, opinions and data contained in all publications are solely those of the individual author(s) and contributor(s) and not of MDPI and/or the editor(s). MDPI and/or the editor(s) disclaim responsibility for any injury to people or property resulting from any ideas, methods, instructions or products referred to in the content.